remote sensing

MDPI

Article

A Multi-Temporal Small Baseline Interferometry Procedure Applied to Mining-Induced Deformation Monitoring

Riccardo Palamà [1,*], Michele Crosetto [1], Jacek Rapinski [2], Anna Barra [1], María Cuevas-González [1], Oriol Monserrat [1], Bruno Crippa [3], Natalia Kotulak [2], Marek Mróz [2] and Magdalena Mleczko [2]

[1] Geomatics Research Unit, Centre Tecnologic de Telecomunicacions de Catalunya (CTTC-CERCA), Avg Gauss 7, E-08860 Barcelona, Spain; mcrosetto@cttc.cat (M.C.); abarra@cttc.cat (A.B.); mcuevas@cttc.es (M.C.-G.); omonserrat@cttc.cat (O.M.)
[2] Faculty of Geoengineering, University of Warmia and Mazury in Olsztyn, 10-720 Olsztyn, Poland; jacek.rapinski@uwm.edu.pl (J.R.); natalia.ostrowska@uwm.edu.pl (N.K.); marekm@uwm.edu.pl (M.M.); magdalena.mleczko@uwm.edu.pl (M.M.)
[3] Department of Geophysics, University of Milan, Via Cicognara 7, I-20129 Milan, Italy; bruno.crippa@unimi.it
* Correspondence: rpalama@cttc.es

Abstract: This work addresses a methodology based on the interferometric synthetic aperture radar (InSAR) applied to analyze and monitor ground-motion phenomena induced by underground mining activities in the Legnica-Glogow copper district, south-western Poland. The adopted technique employs an InSAR processing chain that exploits a stack of Sentinel-1 synthetic aperture radar (SAR) images using a small baseline multitemporal approach. Interferograms with small temporal baselines are first selected, then their network is optimized and reduced to eliminate noisy data, in order to mitigate the effect of decorrelation sources related to seasonal phenomena, i.e., snow and vegetation growth, and to the radar acquisition geometry. The atmospheric disturbance is mitigated using a spatio-temporal filter based on the nonequispaced fast Fourier transform. The estimated displacement maps and time series show the effect of both linear and impulsive ground motion and are validated against global navigation satellite system (GNSS) measurements. In this context, a significant threat to the built environment is represented by seismic tremors triggered by underground mining activities, which are analyzed using the proposed method to integrate the information gathered by in situ seismometer devices.

Keywords: persistent scatterer interferometry; Sentinel-1; mining-induced ground deformation; MTInSAR

Citation: Palamà, R.; Crosetto, M.; Rapinski, J.; Barra, A.; Cuevas-González, M.; Monserrat, O.; Crippa, B.; Kotulak, N.; Mróz, M.; Mleczko, M. A Multi-Temporal Small Baseline Interferometry Procedure Applied to Mining-Induced Deformation Monitoring. *Remote Sens.* **2022**, *14*, 2182. https://doi.org/10.3390/rs14092182

Academic Editor: João Catalão Fernandes

Received: 16 March 2022
Accepted: 29 April 2022
Published: 2 May 2022

1. Introduction

Underground mining activity often triggers substantial ground surface displacements in both vertical (subsidence) and horizontal directions. The deformation values may range from a few millimeters to a few hundred millimeters depending on a multitude of factors, such as the extraction technology, the mined material, and the geological characteristics of the area. Accordingly, the geographical extension of the area affected by terrain deformation varies, depending mainly on the depth of the excavation room, with deformation cone footprints ranging from a few hundreds of meters to kilometers. On the other hand, the temporal deformation behavior changes the deformation rate caused by small collapsing events or heavy mining-induced seismic tremors, which are considered the most serious threat to the built environment due to their unpredictable nature [1,2]. Such deformation phenomena can cause severe damage to buildings and infrastructures; thus, accurate monitoring of the affected area is necessary and often compulsory. In particular, the presence of seismic tremors and the wide extension of the affected areas makes necessary the development of monitoring tools that can deliver wide-area results with a short revisit time. The Lower Silesian region, in south-western Poland, experiences intense copper mining

activity operated by the KGHM company. In particular, mining activity is concentrated in the Legnica-Glogow copper district (LGCD) and has caused an impact on both the built environment and infrastructures due to ground movement of both linear and pulse-based types, triggered by underground excavations [3–7].

Monitoring the deformation phenomena induced by mining activity is traditionally performed by leveling tools, global navigation satellite system (GNSS) measurements [8], terrestrial laser scanning [9], and accelerometers and seismometers to study seismic tremors. However, the aforementioned tools present significant drawbacks, i.e., (i) their deployment is time-consuming, (ii) they require frequent maintenance, and (iii) they mainly produce point measurements and, thus, can only be used to study small deformation areas. Recent decades have seen a growing interest in synthetic aperture radar (SAR) techniques—both satellite-borne and ground-based—for the wide-area monitoring of deformations of either natural or anthropogenic origin, including mining-induced ground motion. In particular, interferometric synthetic aperture radar (InSAR) is a technique linking SAR and interferometry, which finds application in a wide variety of research fields, such as digital elevation model generation, ground surface deformation mapping, the monitoring of critical infrastructures, and others [10]. In the past two decades, significant advances have been made in the InSAR field with the increasing availability of satellite-borne all-weather SAR data with improved spatial resolution and coverage [10,11], enabling the continuous monitoring of the Earth's surface. Progress has been made in developing the InSAR technology and increasing its potential for detecting and mapping sub-centimeter surface deformation. Differential InSAR (DInSAR) processes the SAR interferograms, calculated from SAR images acquired at different times, to extract the temporal evolution of the interferometric phases, which is related to the changes in the illuminated surface displacement along the radar line-of-sight (LOS). Furthermore, persistent scatterer InSAR (PSInSAR) and distributed scatterer InSAR (DSInSAR) techniques have been developed to select temporally coherent scatterers, extract reliable phase contributions, and mitigate the detrimental effect of phase noise on the performance of the phase unwrapping algorithms [12,13]. The selection of persistent scatterers (PSs) in SAR differential interferograms is usually performed by simple thresholding, using metrics such as interferometric coherence or amplitude dispersion. However, challenges have been faced when developing robust PS solutions due to the decorrelation between SAR complex images, resulting in poor interferometric phase stability. Several approaches have been proposed to decrease the decorrelation among interferometric phases, such as interferogram filtering [14], or the use of multitemporal techniques, which form a network of multi-baseline interferograms aimed at decreasing the effect of noisy interferograms [15]. Advanced solutions were proposed to select PSs and distributed scatterers (DSs) based on statistical homogeneity tests [16] and combining interferogram filtering and small-baseline (SBAS) interferogram network optimization [17–19], which made feasible automated deformation monitoring over wide areas, also thanks to the increasing computing resources that have become available over time [20–24]. The authors of [18] outlined a method to build a minimum spanning tree structure implemented by first defining a distance function, which is modeled using interferometric coherence: this method has proved particularly effective in addressing coregistration errors. In a previous study [19], the interferogram network was defined pointwise by a metric that, for each point, calculated the weighted sum of the interferometric phases wherein the weights were calculated from the spatial coherence values.

Radar interferometry has been employed to monitor mining-induced deformation in many works available in the literature. In one study [25], multitemporal InSAR was used to monitor salt-solution mining, whereas coal mining was studied in [26] by integrating DInSAR and SBAS techniques and, in [27], using high-resolution TerraSAR-X images. The area analyzed in this work is located in the Lower Silesian region, south-western Poland, and is affected by intense copper mining activity. The resultant mining-induced tremors have been studied using DInSAR techniques in a previous study [3] regarding the Rudna mine. In contrast, the Legnica-Glogow copper district has been addressed in a recent

couple of studies [6,7]. In particular, Antonielli et al. [6] analyzed the mining-induced land subsidence and tremors using a PSInSAR approach combined with DInSAR, using Sentinel-1 data over 4.5 years (autumn 2014 to spring 2019). The results showed the presence of significant displacements in both vertical and horizontal directions in the main mining district near the towns of Polkowice, Moskorzyn, and Tarnowek; however, this denoted a loss of coherence, thus yielding a reduced persistent scatterer coverage at the center of the differential interferograms included in the deformation areas.

In this work, we adopt a multitemporal InSAR (MTInSAR) methodology to study terrain deformation phenomena in the Legnica-Glogow copper district, enabling a robust monitoring routine on both the slow and fast phenomena (i.e., tremors) that affect the area. The employed datasets are from Sentinel-1 A/B SLC SAR images collected from September 2019 to September 2020 on both ascending and descending trajectories. In particular, we adopt an SBAS approach based on a simplified procedure to form a sub-optimal interferogram network, aiming at eliminating interferograms with a low coherence while preserving the temporal resolution. The adopted method is similar to other proposed approaches, as it aims to eliminate the branches of the interferogram network with low quality [17–19]. The processing software employed for image coregistration, interferogram generation, phase unwrapping, and time-series extraction is part of the PSI processing chain available at the Geomatics Research Unit of the Centre Tecnològic de Telecomunicaciones de Catalunya (CTTC) [28,29]. Particular attention is paid to the mitigation of atmospheric phase screen (APS) disturbance in the unwrapped interferograms, i.e., the phase delay due to the non-uniform refractivity of various layers of the atmosphere, in particular the troposphere. The refractive index of the troposphere is influenced by meteorological factors, such as water vapor, temperature, and pressure, which change over time and space, making the APS a spatio-temporal non-stationary signal [12,13,30,31]. The APS is generally divided into two components, i.e., turbulent mixing and vertical stratification. The latter is related to changes in atmospheric refractivity due to the terrain's altitude, whereas the former is common to all the radar scenes. As the area analyzed in this work is rather flat, with altitude values ranging between 100 m and 500 m, we consider the stratified delay component of the APS to be negligible. Hence, only the turbulent mixing component is considered. If not mitigated, the APS signal often introduces fictitious components into the unwrapped interferograms that may be interpreted erroneously as deformations. Previous works (e.g., [31,32]) have shown that the atmospheric signal presents a high spatial autocorrelation and low temporal correlation. Hence, the APS can be estimated by combining a spatial low-pass filter and a temporal high-pass filter. This data-driven approach is expected to detect temporally correlated surface deformations. In this work, we propose a data-driven APS estimation technique that estimates the APS for the non-uniform grid of unwrapped differential interferometric phases of the selected PSs. The spatial interpolation is replaced by a nonequispaced Fourier transform (NFT) [33], which enables a spatial low-pass filter directly in the spatial frequency domain.

Additionally, the final product obtained via the proposed processing is compared with in-situ data collected by four GNSS stations located in areas affected by severe deformation phenomena. Besides, co-seismic differential interferograms are analyzed to investigate the seismic events recorded by seismometer devices within the area of interest.

This paper is organized as follows. Section 2 shows the study area and the processed Sentinel-1 SAR SLC image stacks. Section 3 is devoted to describing the multitemporal InSAR methodology employed in this work. The main results of the adopted technique are explored in Section 4, which also contains a comparison between InSAR-LOS and GNSS time-series data, co-seismic interferogram evaluation, and vertical/horizontal component analysis. Section 4 is devoted to the discussion of the main results and findings. Final remarks and future development insights are offered in Section 5.

2. Study Area and Dataset Description

In this work, we analyze SAR SLC images collected by the Sentinel-1 A/B on-board sensors, using the interferometric wide swath (IW) acquisition mode. Vertically polarized transmit-receive (VV) data were analyzed, as they are expected to provide a more extended PS coverage with respect to the other available polarization options (vertical-transmit horizontal-receive, VH). The area of interest (AOI) is located around Polkowice, south-western Poland. As shown in Figure 1, the area consists of urbanized environments, rural areas, bare soil, and forested and vegetated land. In Figure 1, five active mining areas are indicated, i.e., Rudna, Polkowice, Glogów, Lubin-Malomice, and Sieroszkowice. The mining activity causes deformation that extends within the southeast area of Polkowice, also affecting the nearby villages of Biedrzychowa and Pieszkowice. Another major deformation area is located approximately 8 km north of Polkowice, affecting Przesieczna, Borów, Jerzmanowa, Gaiki, and Bądzów. Other deformation areas are located in Parchów (west), Jędrzychów (south), Tarnowek, and Zukow (north-east). In addition, the area surrounding Żelazny Most, a copper mining tailings dam located to the east of Polkowice, is also affected by deformation, which is analyzed in [7]. In order to study the deformation phenomena affecting the AOI, we processed the SAR images collected on both ascending and descending passes, which makes feasible the estimation of the horizontal and vertical deformation components [34]. The analyzed datasets were collected by the Sentinel-1 on-board radar system from September 2019 to September 2020, with an interval of 6 days between two subsequent acquisitions. Sentinel-1 A/B SAR SLC images are available at the European Space Agency (ESA) Open Access Data Hub (https://scihub.copernicus.eu, accessed on 16 March 2022) and NASA's Alaska Satellite Facility platform (https://search.asf.alaska.edu, accessed on 16 March 2022). A summary of the analyzed datasets is available in Table 1. As shown in Figure 1, a network of passive corner reflectors (PCRs) was located within the AOI. PCRs are metallic objects designed to maximize the energy of the radar signal that is backscattered to the transmitter. The standard shape of a PCR is a trihedral (with square or triangular facets), in the case of monostatic radars, a dihedral, or a sphere or cylinder in the case of bistatic radars [35]. A network of GNSS stations is also located within the AOI, which provides robust measurements of the three-dimensional displacement vector. Furthermore, seismometers were utilized to measure the mining-induced tremors affecting the analyzed area, yielding measurements of the acceleration provoked by such events. Table 2 summarizes the locations, acronyms, and proximity of the GNSS and seismometer stations within the AOI. Trimble NET R9 receivers with Trimble Zephyr geodetic antennas were used for GNSS stations. Receiver positions were calculated using double differenced phase observations in reference to stations outside of the mining activity area. REFTEK 130SMHR seismometers were used as seismic stations.

Table 1. Summary of the analyzed datasets.

Feature	Dataset #1	Dataset #2
Pass	Ascending	Descending
Beam Mode	IW	IW
Polarization	VV	VV
Band/Wavelength	C/55.5 mm	C/55.5 mm
Relative Orbit	22	73
Temporal Resolution	6 days	6 days
Sub-swath/Bursts	2/5	2/5
Swath Width	250 km	250 km
Pixel Spacing (range × azimuth)	2.3 m × 13.9 m	2.3 m × 13.9 m
Mid Swath Incidence Angle	39	39
Number of Images	62	62
Monitored Period	5 September 2019–5 September 2020	2 September 2019–8 September 2020
Master Image Orbit/Date	S1B18073/17 September 2019	S1A28845/2 September 2019

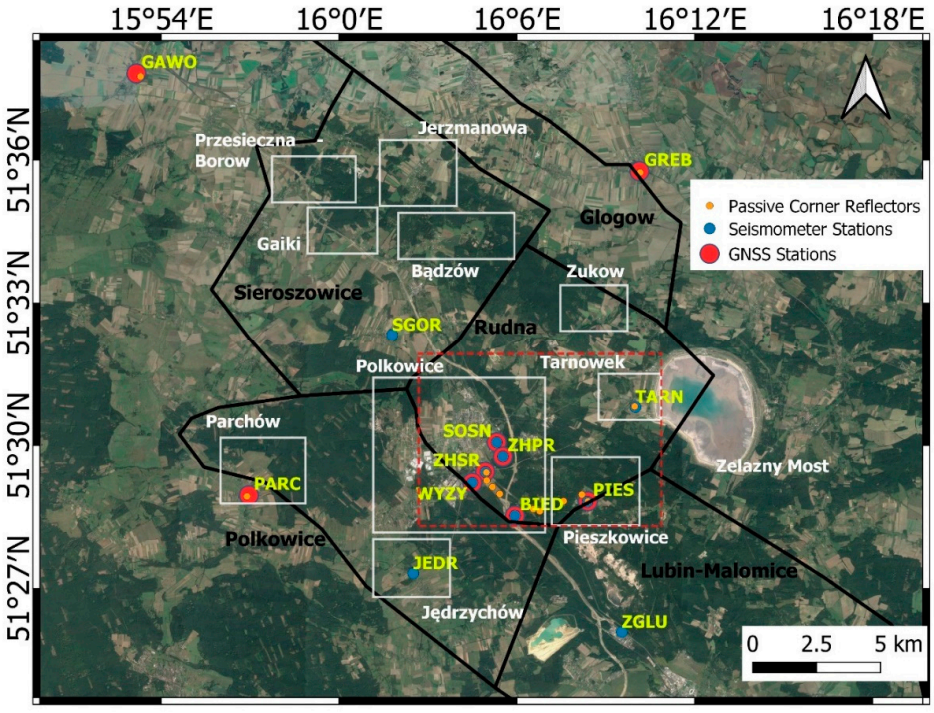

(**a**)

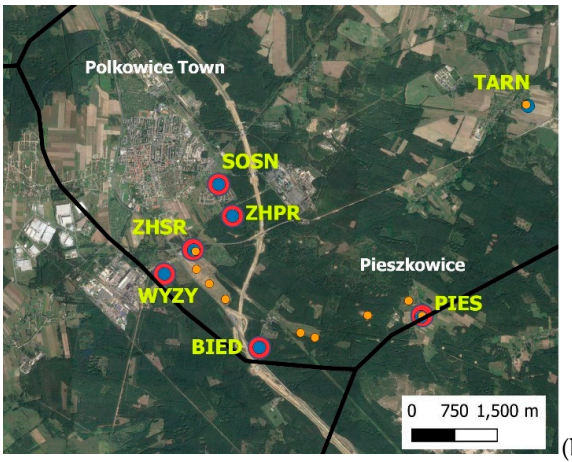

(**b**)

Figure 1. Overview of the area of interest in the Lower Silesian region, Poland (**a**), zoomed in to Polkowice town (**b**). The locations of PCRs are indicated, and the locations and names of the seismometers and GNSS stations. Areas affected by strong deformations are indicated in white; mining areas are indicated in black (from http://dm.pgi.gov.pl/, accessed on 10 March 2022).

Table 2. Location of seismometers and GNSS stations.

Station Name	Location	Lat (°)	Lon (°)	Instrument
PIES	Pieszkowice	51.480275	16.139697	GNSS and Seismometer
SOSN	Polkowice	51.501087	16.088618	Seismometer
ZHPR	Polkowice	51.496135	16.0921	GNSS and Seismometer
ZHSR	Polkowice	51.490735	16.082318	GNSS and Seismometer
WYZY	Polkowice	51.487018	16.074903	GNSS and Seismometer
TARN	Tarnowek	51.513382	16.166647	Seismometer
JEDR	Jędrzychów	51.455227	16.041723	Seismometer
SGOR	Sucha Górna	51.538807	16.029812	Seismometer
BIED	Biedrzychowa	51.475434	16.098855	GNSS and Seismometer

3. Methodology

This section is devoted to illustrating the methodology adopted to process separately the Sentinel-1 SLC SAR images from ascending and descending passes and produce, for each pass, a map of the displacement time series associated with each PS point selected. The ascending and descending maps are then combined to produce vertical and horizontal displacement time-series maps. The workflow of the processing chain employed in this work is shown in Figure 2.

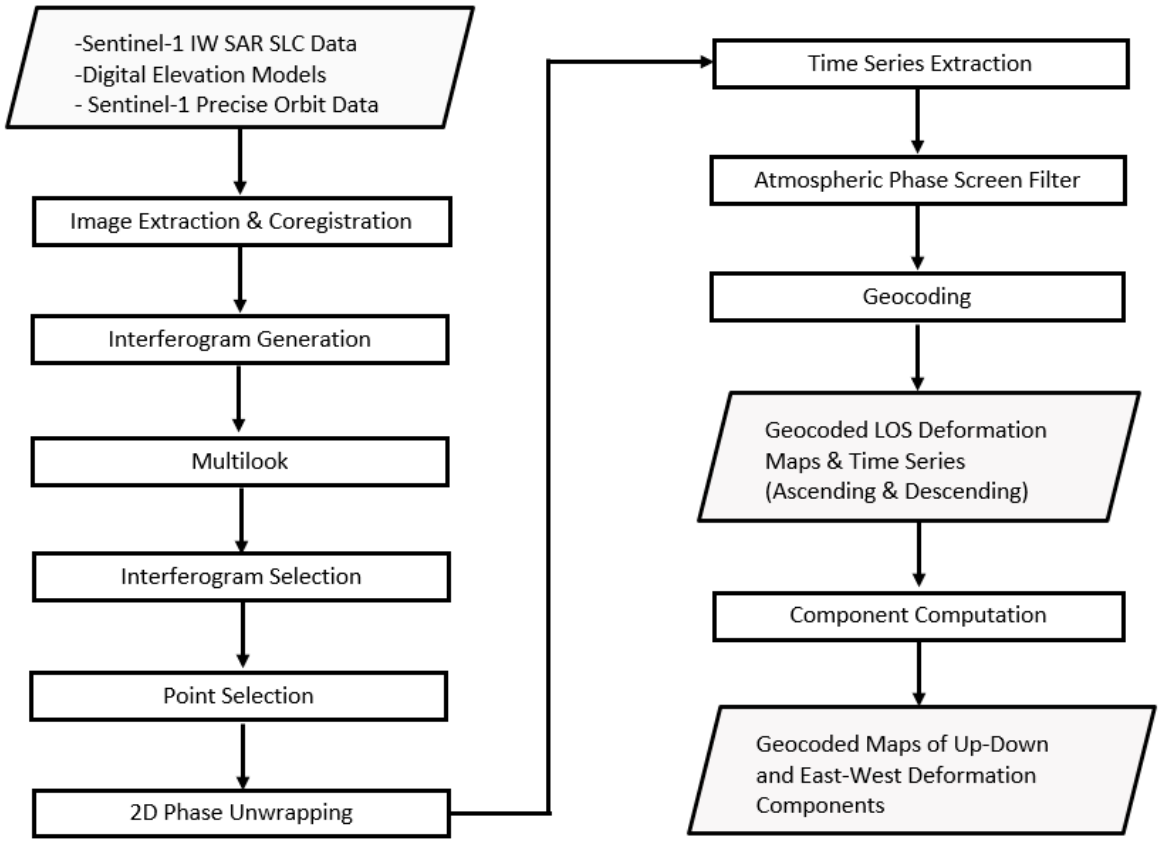

Figure 2. Workflow of the multitemporal MTInSAR processing chain adopted.

3.1. MTInSAR Processing

The main processing steps leading to the estimated deformation maps consist of:

1. *Image Extraction and Coregistration*, where all the SAR images are coregistered against the selected super-master (SM) image.
2. *Interferogram Generation*, achieved using a multitemporal network, with temporal baselines ranging from 6 to 42 days.
3. *Multi-looking*, where multiple looks are generated using a rectangular window whose azimuth and range lengths are represented by Laz and Lrg, respectively. This operation is performed in order to reduce the phase noise in the interferograms, with the cost of reducing the spatial resolution. In this work, we set Laz = 2 and Lrg = 10, obtaining a pixel size of about 28 m in azimuth and 23 m in range.
4. *Coherence Computation*, i.e., for each interferogram, the interferometric coherence [30] is computed using a 2-by-2 window.
5. *Interferogram Selection*. The interferograms generated in step 2 form a multitemporal network, where each master image is associated with each slave image through an edge that is represented by the interferogram itself. Typical interferometric techniques make use of the full interferogram network, formed by all the interferograms whose temporal baseline falls between the predefined minimum and maximum values. However, selecting interferograms with suitable interferometric properties is of paramount importance to ensure the good performance of the following stages, i.e., point selection, phase unwrapping, and time-series extraction. At the same time, eliminating some of the interferograms from the network decreases the redundancy of the images forming those interferograms. In the following, we define image redundancy as the number of interferograms in the network involving the selected image, either as master or slave. Images with low redundancy have reduced connections with the other images of the network, which can be due to the radar geometry, e.g., large perpendicular baselines, or to seasonal phenomena, e.g., the presence of snow or vegetation growth [36]. This study employs an interferogram selection method that adopts two constraints, i.e., a minimum interferometric coherence and a minimum image redundancy. All the interferograms whose average spatial coherence, $\overline{\gamma}$, is lower than a defined threshold, $\overline{\gamma}_{min}$, are eliminated. Then, all the images whose redundancy, ρ, is lower than a minimum value, ρ_{min}, are also eliminated. In fact, removing some images causes the elimination of those interferograms they are involved in, which makes an iterative procedure necessary so that they converge to a reduced interferogram network, for which the two conditions, i.e., minimum average coherence and minimum image redundancy, are met. We observe that previous research in the literature has already adopted a similar criterion by setting a threshold on the perpendicular baseline separating each image from the SM or separating each pair of images forming an interferogram [17]. We adopt the average spatial coherence of each interferogram to account also for the aforementioned seasonal decorrelation phenomena. Additionally, minimum image redundancy is a further improvement that we adopt.
6. *Point Selection*. Once the interferograms have been selected, point selection is performed by setting a threshold over an equivalent temporal coherence [17], which is calculated as:

$$\Omega(P) = \frac{1}{M}\left|\sum_{k=1}^{M} exp[j(\varphi_k(P) - \varphi_{k,LP}(P))]\right| \quad (1)$$

where the index P identifies a pixel, M is the number of interferograms selected in the previous step, k is the interferogram index, φ_k is the wrapped interferometric phase of the k-th interferogram, and $\varphi_{k,LP}$ is the low-pass estimate of the wrapped interferometric phase of the k-th interferogram. The calculation is performed on the wrapped interferograms. First, the estimation of the spatial low-pass interferometric phase is computed using a boxcar averaging window (in this work, we used a 2-by-2 window), then the spatial low-pass phase is subtracted as modulo-2π from the original interferometric phase, giving a high-pass estimate of the interferometric phase. For each pixel, the high-pass phasors are averaged coherently in order to mitigate the

effect of the phase noise, then, the module of the resultant vector is computed. The values of the equivalent temporal coherence range between 0 and 1. The higher the value of the equivalent temporal coherence, $\Omega(P)$, the more coherent that pixel. This multitemporal point selection criterion highlights the overall behavior of the interferometric phases of a pixel, ignoring isolated noisy interferograms that can otherwise hinder the selection of a highly coherent pixel.

7. *Phase Unwrapping*. The interferometric phases of the selected points are bounded within an interval of 2π; thus, in order to generate an accumulated phase time series, previous phase unwrapping is necessary. This problem has been tackled by several authors in the literature [37] and is considered to be one of the most critical challenges in InSAR technology. We adopt a 2D phase unwrapping procedure, based on a minimum cost flow criterion [38].
8. *Time Series Generation*. Once the phase-unwrapped interferograms have been produced, they are processed using an inversion technique based on a least mean square (LMS) optimization routine to extract the accumulated phase time series for each selected point. This step is described in [29] and produces a 2D (spatial) plus 1D (temporal) grid of points.

3.2. Atmospheric Phase Screen Filter

The estimation and removal of the APS is usually performed following either a model-based or a data-driven approach. Model-based approaches exploit meteorological data to calculate the refractive index of the atmosphere and build a model of the APS (that is then subtracted from the data), whereas data-driven approaches estimate the APS directly from the data, applying simple APS models. In this work, we employ a data-driven approach that models the APS as a spatial low-pass and temporal high-pass signal. We indicate $\phi(x, y, i)$ as the i-th unwrapped phase value of the point, with coordinates (x, y), being i, the temporal index. The general model of (x, y, i) can be summarized by:

$$\phi(x, y, i) = \phi_{DEFO}(x, y, i) + \phi_{RTE}(x, y, i) + \phi_{APS}(x, y, i) + \phi_{OE}(x, y, i) + \phi_N(x, y, i) \quad (2)$$

where $\phi_{DEFO}(x, y, i)$ is the component related to terrain deformation, $\phi_{APS}(x, y, i)$ is related to the atmospheric phase screen, and $\phi_{OE}(x, y, i)$ is the orbital error component. The terms $\phi_{RTE}(x, y, i)$ and $\phi_N(x, y, i)$ represent the residual topographic error and noise, respectively, and are assumed here to be negligible, due to the almost flat topography of the area of interest.

In this work, the APS is modeled as a spatio-temporal signal with a high spatial correlation and a low temporal correlation, thus reducing its estimation to two subsequent steps, a spatial low-pass (SLP) filter, and a temporal high-pass (THP) filter.

The orbital error component, $\phi_{OE}(x, y, i)$, if present, usually appears as a 2D linear term in the interferograms, which can be reasonably considered as an SLP component. In other words, even if the orbital error component is not physically related to the APS, its mathematical model can be reasonably included within the mathematical model of the APS. Hence, the adopted APS filter is expected to also mitigate the orbital error component, if present. It should be noted that for the datasets analyzed in this work, we have not noticed the presence of any 2D linear term in the interferograms, due to the high precision of the Sentinel-1 orbits.

The SLP filter is performed in the spatial frequency domain. As mentioned above, for each date, i, the input data $\phi(x, y, i)$ are distributed on a non-uniform two-dimensional grid, whose size is $N \times L$. In other words, being (x, y) the spatial coordinates of a pixel, the values of x and y are non-uniformly distributed within the interval $[0, N-1]$ and $[0, L-1]$, respectively. The NFT computes the two-dimensional spectrum of $\phi(x, y, i)$, $\phi(\xi, \nu, i)$, where ξ and ν are uniformly distributed within $[-0.5, 0.5]$ with sampling intervals of $1/N$ and $1/L$, respectively. The NFT is an extension of the classical Fourier transform, addressing the case that the sample support is not uniform. An efficient version of the NFT has been proposed in the form of nonequispaced fast Fourier transform (NFFT),

with efficient implementations in various interfaces [39]. A preliminary illustration and evaluation of the proposed APS filter are addressed in a small area in [40], together with a performance comparison with a traditional two-dimensional convolutional filter. The NFFT procedure can be summarized as two main steps, an interpolation followed by an FFT. The interpolator has been implemented efficiently using a Sobolev kernel ([8] pp. 18–19). After careful analysis, we set the parameters of the Sobolev weights as $\alpha = 2$, $\beta = 0.1$ and $\gamma = 0.01$. The filtering is performed in the frequency domain by multiplying $\phi(\xi, \nu, i)$ in a bidimensional Butterworth filter function:

$$H_{SLP}(\xi, v) = \frac{1}{\sqrt{1 + \left(\frac{\xi^2 + v^2}{d_c^2}\right)^n}} \tag{3}$$

where d_c is the spatial cutoff factor and n is the filter order. Lower values of d_c yield a more selective filter, rejecting a larger portion of the image spectrum, but also yield a smoother filtering function. The inverse nonequispaced FFT (INFFT) is applied to the filtered spectrum $\phi_{SLP}(\xi, v, i) = \phi(\xi, v, i) \cdot H_{SLP}(\xi, v)$; to obtain the SLP component of the input data, $\phi_{SLP}(x, y, i)$. The THP filter is applied to the SLP component using the one-dimensional NFFT, which also ensures good performance in cases where the temporal sampling is not uniform. In the case analyzed in this work, the sampling interval was constant, corresponding to the 6-day temporal baseline of the Sentinel-1 constellation during the monitored period. The estimate of atmospheric phase noise is obtained by computing the THP component of $\phi_{SLP}(x, y, i)$, which is achieved by computing the residual of its temporal low-pass (TLP) component. The frequency response of the one-dimension low-pass Butterworth filter is given by:

$$H_{TLP}(f) = \frac{1}{\sqrt{1 + \left(\frac{f}{f_c}\right)^{2m}}} \tag{4}$$

where f_c is the temporal cutoff frequency and m is the temporal filter order. Once indicated as $\phi_{SLP,TLP}(x, y, i)$, the output of the TLP filter, the APS estimate is given by:

$$\hat{\phi}_{APS}(x, y, i) = \phi_{SLP}(x, y, i) - \phi_{SLP,TLP}(x, y, i) \tag{5}$$

The final output of this step is a grid of deformation time series, obtained separately for the ascending and descending stacks of images. The displacement of the point with coordinates (x, y) at epoch i, D_i, is calculated as:

$$D_i = \frac{\lambda}{4\pi}\left[\phi(x, y, i) - \hat{\phi}_{APS}(x, y, i)\right] \tag{6}$$

where λ is the radar wavelength, approximately equal to 55.5 mm for the Sentinel-1 onboard radar system. It should be noted that interferometric techniques are phase-based, which does not provide absolute measurements; therefore, the initial displacement value is taken as a reference, i.e., the first date is set to zero and the rest of the dates are referenced to it.

3.3. Component Extraction

The last step computes the vertical and horizontal displacement components from the LOS deformation components extracted from the ascending (D_A) and descending (D_D) data (Equation (7)). The general model gives D_A and D_D in the three-dimensional space as a function of the vertical (up-down, UD) and horizontal components. The horizontal component is itself projected in two directions, i.e., the east-west (EW, D_{EW}) and north-south (NS, D_{NS}) ones:

$$\begin{aligned} D_A &= D_{UD}\cos\theta_A - D_{EW}\sin\theta_A\sin\alpha_A - D_{NS}\sin\theta_A\cos\alpha_A \\ D_D &= D_{UD}\cos\theta_D - D_{EW}\sin\theta_D\sin\alpha_D - D_{NS}\sin\theta_D\cos\alpha_D \end{aligned} \quad (7)$$

where α_A and α_D are the azimuth angles of ascending and descending trajectories, respectively. θ_A and θ_D are the look angles in ascending and descending trajectories, respectively. The values of these angles are shown for the analyzed datasets in Table 1. As most SAR satellite sensors, including Sentinel-1, have flight trajectories almost parallel to the NS direction, it is often not possible to retrieve the NS deformation component. Hence, in this work, the NS deformation component associated with satellite data is ignored, thus the vertical and horizontal displacement components are calculated—by inverting Equation (7)—as follows:

$$\begin{aligned} D_{UD} &= \frac{\sin\theta_D\cos\alpha_D D_A - \sin\theta_A\cos\alpha_A D_D}{\cos\theta_A\sin\theta_D\ \cos\alpha_D - \cos\theta_D\sin\theta_A\ \cos\alpha_A} \\ D_{EW} &= \frac{\cos\theta_D D_A - \cos\theta_A D_D}{\cos\theta_A\sin\theta_D\ \cos\alpha_D - \cos\theta_D\sin\theta_A\ \cos\alpha_A} \end{aligned} \quad (8)$$

The conversion of the D_A and D_D LOS maps to vertical and horizontal deformation maps is performed using the method described in [41]. The adopted method forms a two-dimensional grid with a predetermined coarse resolution (in this work we use 40×40 m^2 pixels), in order to ensure that two corresponding points in the D_A and D_D maps fall into the same pixel of the UD and EW maps. The computation of the UD and EW components is then performed as per Equation (8).

4. Results

This section is devoted to a description of the main results obtained using the processing chain described in Section 3 on the SAR SLC datasets listed in Section 2. The performance of the interferogram and point selection methods is analyzed in Section 4.1, and the main results regarding the displacement along the D_A and D_D LOS are illustrated in Section 4.2, whereas the UD and EW deformation components are analyzed in Section 4.3. It should be noted that the analyzed area represents a sub-area of one burst for both ascending and descending data. For the ascending data, we selected an area of 970 range (rg) bins by 720 azimuth (az) bins, whereas for the descending data, the area was 810 (rg) by 730 (az).

4.1. Interferogram and Point Selection

The initial interferogram network was generated using temporal baselines from 6 to 42 days, separated by an interval of 6 days, i.e., the revisit time of the Sentinel-1.

The interferogram network is represented in this paper using a graph, where each image is associated with a point in the two-dimensional plane given by the temporal and perpendicular baselines with respect to the SM image (i.e., the image taken as a reference for coregistration). The graph of the full network for the Sentinel-1 ascending datasets is shown in Figure 3a. The original network consists of 399 interferograms involving 62 images, with a maximum redundancy of 14 achieved in the middle of the monitored period. The interferogram selection method described in Section 3.1 yields a reduced network of 298 interferograms for 61 images, as shown in Figure 3b. This result was obtained using a minimum average coherence ($\overline{\gamma}_{min}$) of 0.2 (typical values are included between 0.15 and 0.55) and a minimum image redundancy (ρ_{min}) of 4. These values were tuned by a trial and error procedure to eliminate the maximum number of interferograms while keeping as many images as possible, in order not to decrease the temporal resolution for the time-series analysis. We observe that most of the eliminated interferograms are concentrated in two main periods, which are January–February, and June–August. These periods are associated with the presence of two seasonal sources of decorrelation, i.e., snow in the winter months and vegetation growth during spring, reaching its maximum at the end of June.

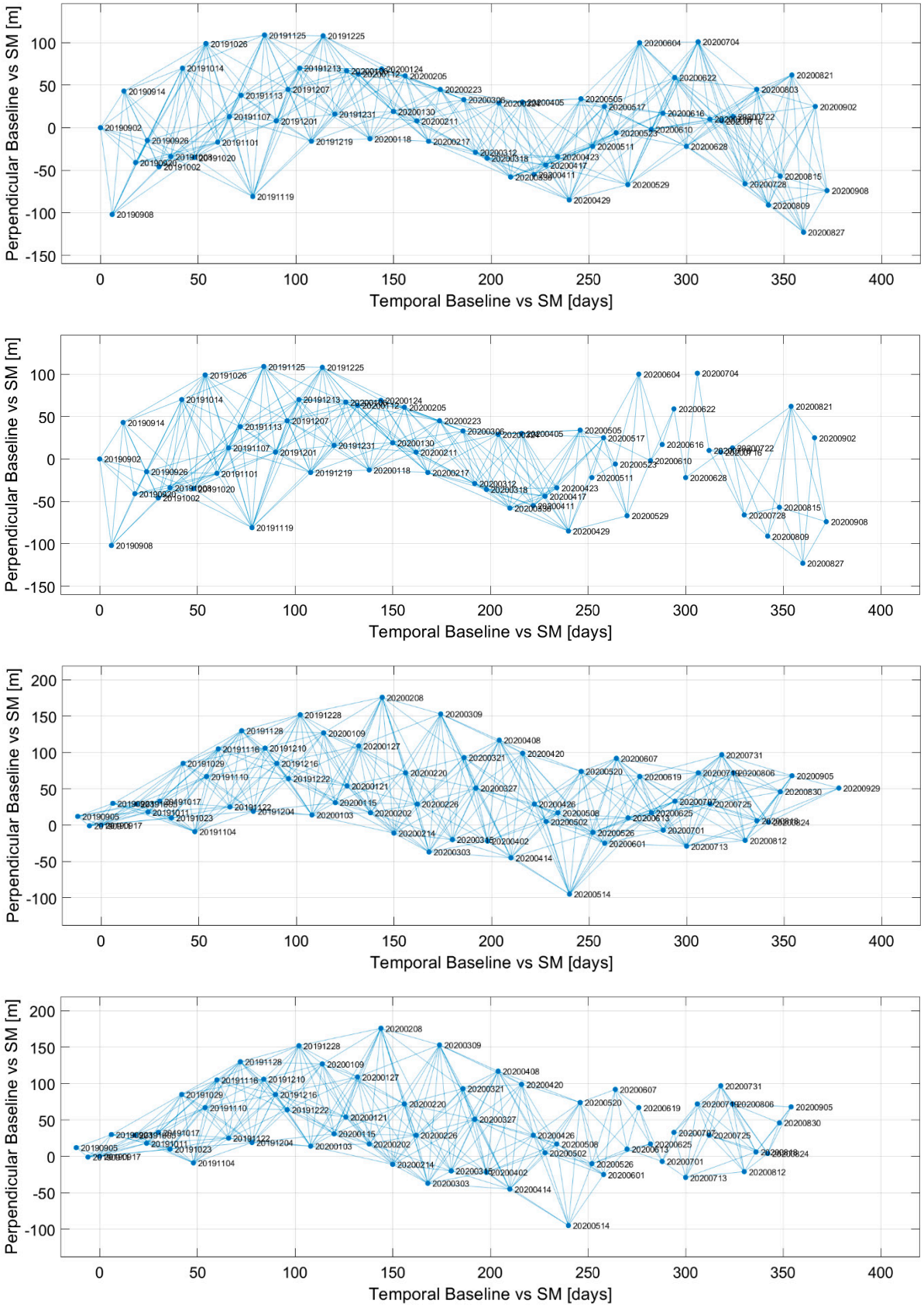

Figure 3. Small baseline interferogram network, full (**a**) and reduced (**b**) for Sentinel-1 ascending data, full (**c**) and reduced (**d**) for descending data, represented in the plane given by the temporal/perpendicular baselines with respect to the Super-Master image. Sentinel-1.

The full and reduced network graphs of the descending datasets are represented in Figure 3c,d, respectively. For the descending data, the full interferogram network consists of 399 interferograms for 62 images, whereas the reduced network has 327 interferograms for 61 images, obtained by setting $\overline{\gamma}_{min} = 0.2$ and $\rho_{min} = 3$. The descending data showed generally higher interferometric coherence with respect to ascending ones, shown by the larger number of interferograms in the reduced network. On the other hand, the values of the SM-referenced perpendicular baselines spanned a larger interval in descending data ([–100, 160] m) than in the ascending ones ([–100, 100] m). However, seasonal decorrelation phenomena also occur during winter and spring–summer in the descending data.

Following the interferogram selection, we performed point selection using the thresholding criterion, which is the 6th step of the processing chain described in Section 3.1. Figure 4a,b show the maps of the equivalent temporal coherence (Equation (1)) calculated over the descending data for the full and reduced interferogram networks. A threshold of 0.8 was applied to the Ω maps to select the PS points that enter the following phase-unwrapping stage. Figure 5 shows the histograms of the Ω values obtained over the ascending and descending data for both the reduced and full interferogram networks. The histograms are shown in the form of an empirical probability density function (pdf), i.e., by normalizing the bin counts on the total number of samples and bin width. We observe that such histograms present two peaks, i.e., the distribution of the Ω values is bimodal, where the first peak is located at $\Omega \approx 0.3$ for all the data and network configurations. This peak is related to low-coherence pixels, including water, vegetated and forested areas, and is not modified by the interferogram selection procedure. On the other hand, the second peak is influenced by the interferogram selection; as for the ascending data (Figure 5a), it is approximately equal to 0.58 for the full network and 0.7 for the reduced network, respectively. A similar gap is observed in Figure 5b for the descending data, ranging from 0.58 to 0.64, approximately. The elimination of noisy and low-coherence interferograms and decorrelated images makes the second peak of the Ω distribution increase, meaning that a larger number of points can be selected. This can be justified by the fact that the points belonging to the higher part of the Ω distribution suffer from isolated decorrelation phenomena. A threshold of 0.8 was applied to select the PS points; the results are shown graphically in Figure 5 and numerically in Table 3. We observe that the greater increase in the number of selected points is achieved in the ascending case, ranging from 3.83% for the full network to 7.97% for the reduced network. For the descending data, the number of selected points for the full network (4.8%) is higher than the ascending ones, yielding a lower increase obtained using the reduced network (approximately 3%). A possible cause of this behavior is that descending data for the analyzed datasets have higher coherence than ascending ones, which is also reflected in the higher number of the selected interferograms. However, the interferogram selection procedure allows an equalization between the number of selected points of the two datasets.

Table 3. Percentage of selected points (threshold = 0.8).

	Ascending	**Descending**
Reduced Network	7.97%	7.79%
Full Network	3.83%	4.8%

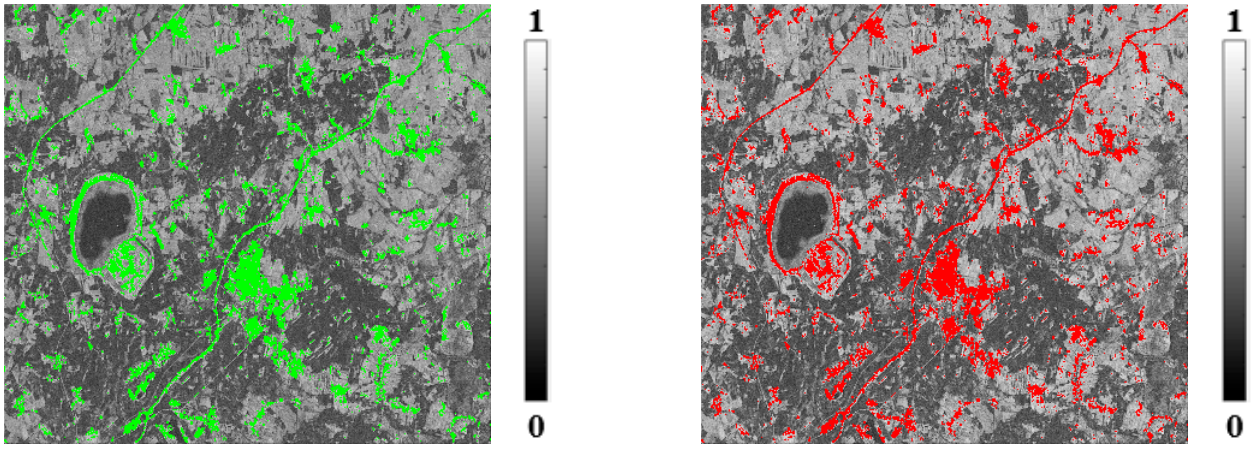

(**a**) (**b**)

Figure 4. Equivalent temporal coherence images computed on ascending and descending data, overlaid with the points selected with a threshold of 0.8. Vertical axis = azimuth, horizontal axis = range. Descending, full (**a**) and reduced (**b**) interferogram network. The green dots in (**a**) and the red dots in (**b**) represent the selected points using a threshold of 0.8, as associated with the histograms in Figure 5b.

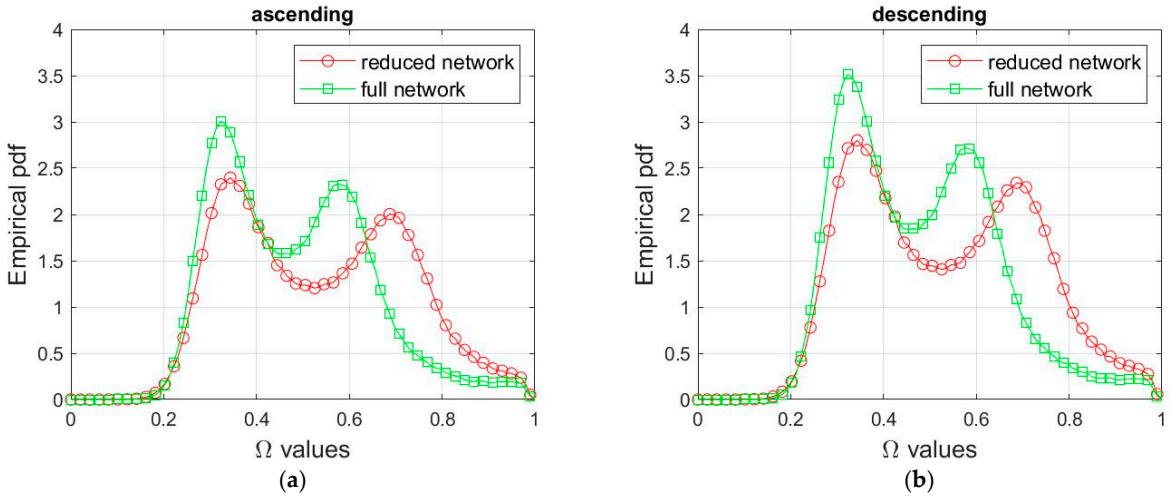

(**a**) (**b**)

Figure 5. Histogram of the equivalent temporal coherence values computed over the whole area of interest, comparing full (green) and reduced (red) interferogram network. Sentinel-1 ascending (**a**) and descending (**b**) data.

4.2. APS Filter

The selected wrapped interferograms were unwrapped over the selected points, then the maps of the accumulated deformation time series were generated according to steps 6 and 7 of the processing chain described in Section 3.1. Mitigation of the APS was performed on the D_A and D_D data using the procedure illustrated in Section 3.2. The input and output of the APS filter applied to the D_D data are shown in Figure 6. The SLP filter was implemented by setting the filter order to 3, whereas the cutoff frequency was set to achieve a spatial averaging over a radius of about 700 m. Regarding the TLP filter, its order was set at 3 and its cutoff frequency was set to achieve a temporal averaging of about 20 days. Although the effect of the APS filter is not clearly noticeable in the maps displayed in Figure 6, a thorough examination reveals the presence of negative patches in the central part of Figure 6a that disappear in the APS-free map (Figure 6b). Besides, the effect of the APS filter is clear in the time series shown in Figure 7, which are associated with points in the vicinity of PCRs near Biedrzychowa and Pieszkowice villages. The APS

filter input shows cyclic fluctuations that are typical for data affected by a turbulent APS, which are corrected by the averaging power of the APS filter. In addition, large jumps are also noticeable in the unfiltered time series in Figure 7a,c, which are realistically not associated with large deformations and are mitigated by the APS filter implemented.

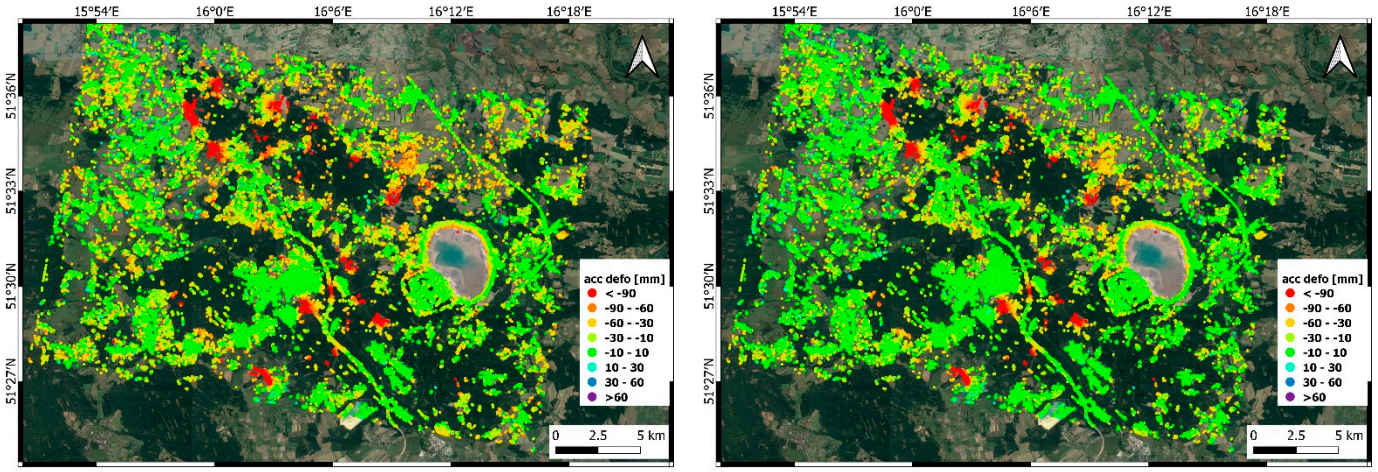

(**a**) (**b**)

Figure 6. Accumulated deformation maps of the Sentinel-1 descending data, input (**a**) and output (**b**) from the APS filter.

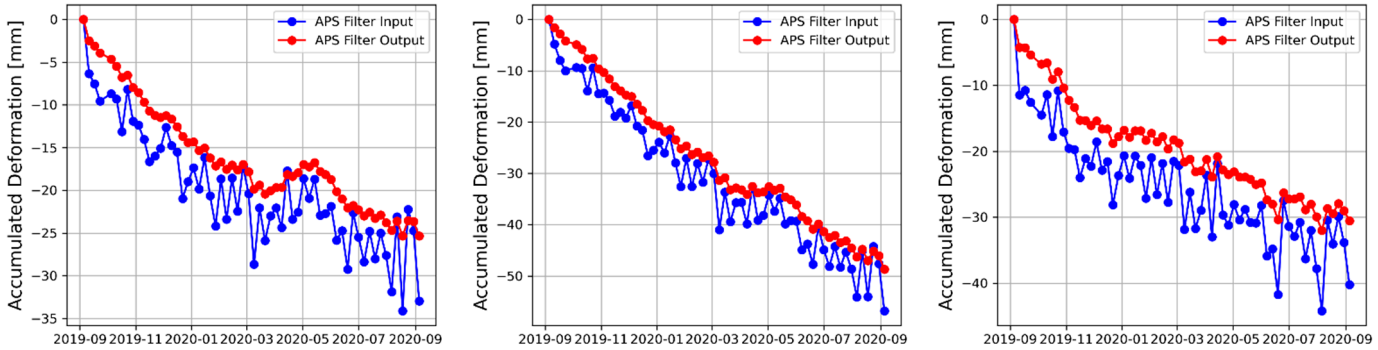

(**a**) (**b**) (**c**)

Figure 7. Accumulated deformation time series comparing the input and output of the APS filter, for three selected points associated with three different passive corner reflectors located in the vicinity of Biedrzychowa (**a**,**b**) and Pieszkowice (**c**).

4.3. Comparison with GNSS LOS-Projected Data

In this section, the LOS displacement time series are compared with the displacement time series measured by four selected GNSS stations, projected onto the LOS directions. The GNSS device measures the 3D displacement vector along the vertical (height), latitude (east-west), and longitude (north-south) directions, which are projected onto the ascending and descending LOSs using the coordinate transformation in Equation (7). This procedure allows a basic validation of the obtained LOS displacement time series, as the 3D GNSS measurements provide a robust benchmark when projected onto the LOS direction.

The locations of the GNSS devices in the AOI are summarized in Table 2 and indicated in Figure 1. Daily observations were processed in a multi-station solution with reference to four GNSS stations located outside of the mine influence area [42]. Processing of daily GNSS observations was carried out with the advanced, scientific Bernese GNSS Software v.5.2, developed at the Swiss Astronomical Institute at the University of Bern (AIUB, Bern, Switzerland). The position of all monitored stations is calculated automatically at

daily intervals. It allows determining the coordinates of GNSS stations, with a horizontal accuracy of about 5 mm and a height accuracy of about 10 mm. These calculations use precise products provided by the IGS (International GNSS Service), such as the clocks and orbits of satellites and the parameters of the Earth's rotation. Daily global ionosphere maps developed by the Center for Orbit Determination in Europe (CODE) analysis center are also necessary, as well as monthly inter-frequency hardware delays (DCB—differential code biases) for satellites and receivers (P1-C1 and P1-P2), also provided by the CODE center.

Raw observations collected by GNSS receivers located at stations are converted to the RINEX (receiver independent exchange system) data exchange format, then they are used in the Bernese module to process the satellite observations. The observations are compiled in 24-h sessions with intervals of 30 seconds. The study uses observations from satellites located at a topocentric height of at least 3° above the horizon, with a weighting of observations using the $cos^2 z$ function, where z is the zenith distance. During the study, the residuals of the phase observations are screened using the iterative method, with a final threshold of 4.0 mm. To determine the receiver and satellite phase center positions, phase center variation (PCV) models derived from IGS calibration are used, depending on the azimuth and the satellite's height above the horizon. The tropospheric delay is determined using the a priori global mapping function (GMF) model for the dry component (dry_GMF), in which tropospheric corrections are determined based on the global pressure temperature (GPT) model and the wet-GMF mapping function. The study also estimates the tropospheric horizontal gradient using the Chen-Herring model. The zenithal tropospheric delay (ZTD) is determined for each station at hourly intervals, while the gradient is estimated as one parameter per day. The ambiguity determination method used in this study depends on the length of the vectors between the stations; the SIGMA method (L1, L1 and L2, L5 and L3) or the QIF method is used.

The processing of satellite observations is performed in several stages. After importing the precise products, the satellite orbits are converted to the tabular format; then, standard orbits are created, taking into account the pole's movement. Afterward, clearing and smoothing of the code observations are performed, followed by preliminary processing of the code observations to synchronize the receiver clocks with the GPS time at the microsecond level. At this stage, the observations stored in RINEX files are checked, and statistics on the number and quality of the collected observations are prepared.

The main part of the GNSS observation development system is based on a relative positioning model with a defined system of vectors of the network under study, with the possibility of changing the geometry of the network depending on the availability of observations collected at reference stations. After checking the geometry of vectors that can be created, based on observations from a given day, the phase observations are initially processed to find and repair the lost parts of the cycle slips and the weighting of erroneous observations due to the multipath of the signal.

The system uses the classic 3-step solution to address the uncertainty of phase measurements, considering each vector separately. First, the float solution with real ambiguities is determined. In the second stage, based on the float solution and the corresponding variance-covariance matrix, the process of determining the uncertainty as to integer values is carried out. Then, the determined ambiguities, which are integers, are used to determine the station coordinates (fixed solution). The final stage of the GNSS observation processing is a network solution with a defined frame of reference, using the minimum constraint solution method. Based on the final stage, the daily coordinates of the points are determined, along with the accuracy characteristics.

In this work, we analyze four different GNSS measurements collected by the PIES (Pieszkowice), WYZY (south of Polkowice), ZHPR, and ZHSR (located within Polkowice urban area) stations. Furthermore, PCRs were installed in the vicinity of the PIES and ZHSR GNSS stations, while each station is also equipped with a seismometer device. Comparisons between the MTInSAR results and GNSS LOS-projected time series are shown in Figure 8 for both ascending and descending trajectories. It should be noted that GNSS data are

available from October 2019, which means that this validation is carried out during an 11-month period; the Sentinel-1 data were analyzed up to September 2020.

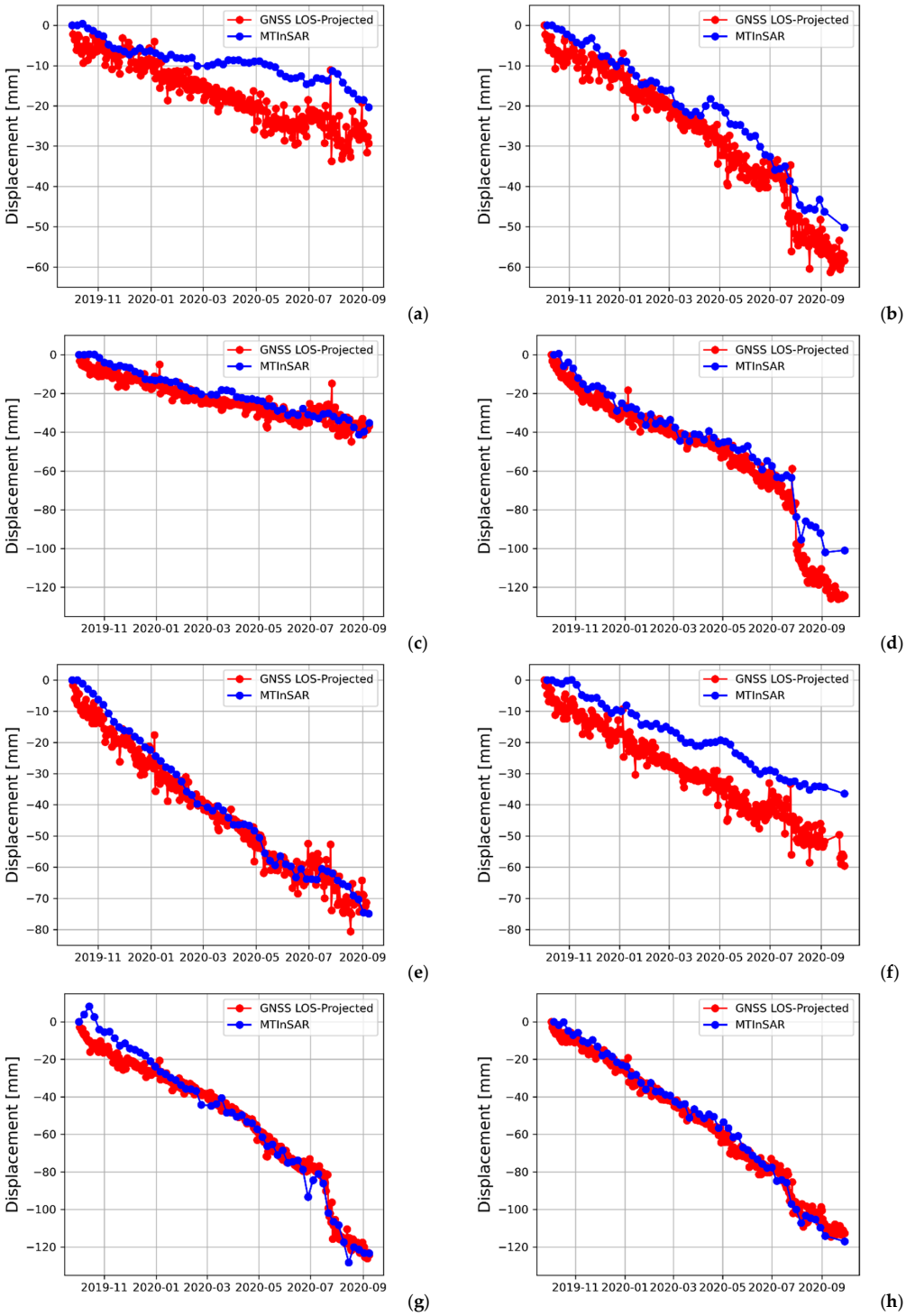

Figure 8. Displacement time series comparing MTInSAR (blue) and GNSS data projected onto the radar line of sight (red), for the points in the vicinity of the GNSS stations: ZHSR, asc (**a**) and desc (**b**); PIES, asc (**c**) and desc (**d**); ZHPR, asc (**e**) and desc (**f**); WYZY, asc (**g**) and desc (**h**).

We observe that the best match is achieved for the WYZY station (Figure 8g,h) which shows a quite significant deformation, of the order of 120 mm. The WYZY time series highlights the presence of a slow deformation trend of about 5 mm/month for both D_A and D_D data. A large discontinuity interrupts both the GNSS and MTInSAR time series

in July 2020, which corresponds to a seismic event recorded at the end of July 2020 (see Table 3). Noticeably, the D_A MTInSAR time series shows a small discontinuity in May 2020, which causes a slight increase in the deformation rate, corresponding to a minor seismic event recorded at the beginning of May 2020. A quite good agreement between MTInSAR and GNSS time series is achieved for the ZHPR station (Figure 8e,f), especially for D_A data, which shows similar deformation rates, whereas the D_D and GNSS data differ by about 9 mm at the end of the monitored period. A slight increase in the D_D deformation rate is noticed in May 2020, probably corresponding to the seismic event recorded in the same period.

The Pieszkowice (PIES) station shows good agreement with the D_A data (a deformation rate of about 3.6 mm/month). The D_D data show a linear deformation rate that is faster than the D_A data (about 6 mm/month) until a large discontinuity occurs in July 2020. Such a discontinuity may be due to a seismic event recorded in July 2020, which is evaluated in the following sub-section through a coseismic interferogram analysis and will be discussed in Section 5. Probably, the abrupt discontinuity occurring in July 2020 caused a loss of coherence in the D_D data, then a phase unwrapping aliasing error, represented by a positive jump in the D_D MTInSAR time series. The ZHSR station shows a good match for D_D data (Figure 8b), the deformation rate of which is about 3.8 mm/month. A small discontinuity (smaller than 10 mm) is recorded by the GNSS data in July 2020, but the results are smoothed in the MTInSAR data. The D_A data show similar shapes in terms of the deformation curves between MTInSAR and GNSS data, but significantly different deformation rates (0.9 mm/month and 3.6 mm/month for MTInSAR and GNSS data, respectively). The observed deviations can be caused by the imperfect overlapping of the detected PS points and GNSS locations, as well as by the smoothing effect of the APS filter.

4.4. Analysis of Seismic Events

The seismic events caused by the underground copper-mining activity are addressed in this sub-section. In order to monitor such events, seismometers were placed at different locations in the AOI (see Figure 1 and Table 2). Table 4 shows the dates of the main recorded events at each station, together with the maximum ground acceleration, the duration, and the values of the GSI-2004 seismicity scale. This scale was proposed by Wodynski and Lasocki [43] to empirically assess the intensity of the seismic events in the Legnica-Glogow copper district and is suited to evaluate the damage caused to buildings and infrastructure [5]. Table 4 shows the events that occurred on three dates, 8 May, 22 July, and 30 July 2020. Most of the recorded events have maximum acceleration values lower than 100 m/s^2 and a GSI scale equal to zero. Two exceptions are the events occurring in the vicinity of the WYZY station (south of Polkowice), on 22 July, lasting for 400 s, with a GSI value of 1, and PIES station (Pieszkowice), on 30 July, with a duration of 1104 s and GSI value of 3. Generally, the WYZY station is the one showing the longest tremors, which may be due to various factors, such as the geology of the terrain, the depth of the excavations, and also (as shown in Figure 1) the proximity of the border between the Rudna and Polkowice mining areas. Other significant tremors were recorded by the ZHSR station (127 s on 8 May, 175 s on 22 July, 158 s on 30 July), Biedrzychowa (max acceleration of 109 m/s^2 and duration of 68 s on 8 May, max acceleration of 52 m/s^2 and duration of 235 s on 30 July). Figure 9 displays a map summarizing the seismic events recorded by the seismometers on 30 July 2020. It could be noted that most events have a strong acceleration and a short duration, except the one occurring in Pieszkowice (PIES), which exhibits rather different behavior.

Table 4. Summary of the main seismic events recorded by the seismometer stations.

Station	Date	Max Acc (m/s^2)	Duration (s)	GSI
BIED	8 May 2020	109.285	68.18089	0
PIES	8 May 2020	85.515	24.9496	0
SOSN	8 May 2020	62.86	64.61115	0
ZHPR	8 May 2020	34.565	59.2062	0
ZHSR	8 May 2020	35.63	127.7952	0
WYZY	8 May 2020	53.78	208.1063	0
TARN	8 May 2020	94.275	23.60922	0
JEDR	8 May 2020	28.11	49.46934	0
SGOR	8 May 2020	55.67	11.89699	0
BIED	22 July 2020	44.895	117.1527	0
PIES	22 July 2020	71.38	22.0104	0
SOSN	22 July 2020	50.18	89.64287	0
ZHPR	22 July 2020	47.22	112.3676	0
ZHSR	22 July 2020	44.98	175.4273	0
WYZY	22 July 2020	50.12	400.6835	1
TARN	22 July 2020	58.845	18.08756	0
JEDR	22 July 2020	36.225	80.76117	0
SGOR	22 July 2020	67.165	25.73893	0
BIED	30 July 2020	51.965	235.0718	0
PIES	30 July 2020	25.475	1104.996	3
SOSN	30 July 2020	50.015	152.8485	0
ZHPR	30 July 2020	56.265	205.3738	0
ZHSR	30 July 2020	52.865	158.3931	0
WYZY	30 July 2020	62.97	149.292	0
TARN	30 July 2020	45.235	167.9423	0
JEDR	30 July 2020	69.79	83.8576	0
SGOR	30 July 2020	80.25	41.24939	0

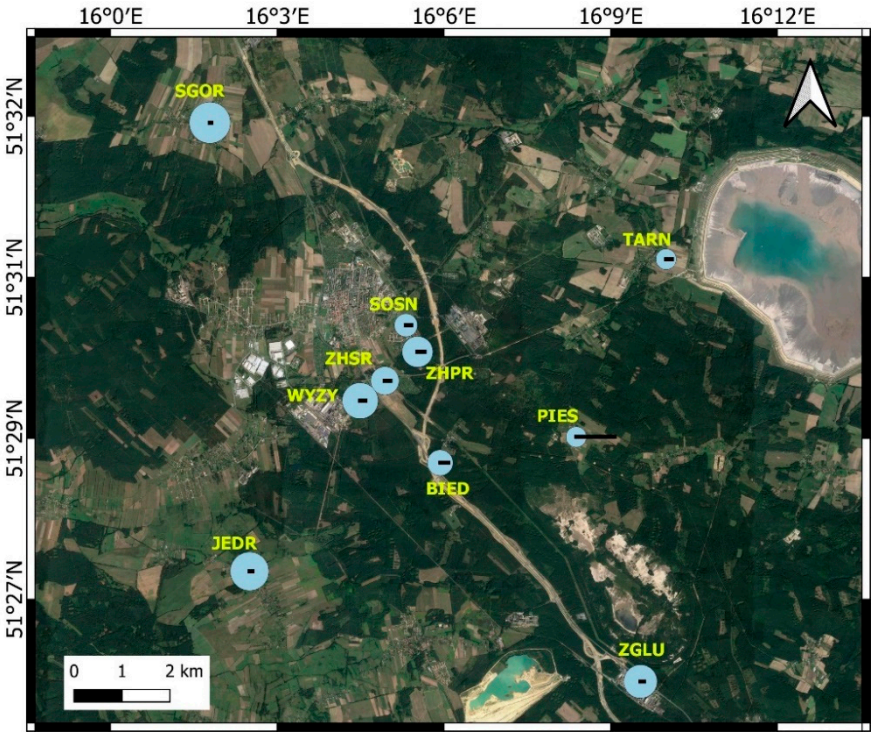

Figure 9. Locations of the seismometers in the AOI. The area of the blue circles is proportional to the maximum acceleration of the seismic event recorded on 30 July 2020, the length of the black bar is proportional to its temporal duration.

The seismic tremor recorded by the WYZY station on 22 July is noticeable in both D_A and D_D time series shown in Figure 8g,h, with an estimated discontinuity of about 25 mm. The study of co-seismic interferograms enables a more accurate deformation estimation, as they are differential interferograms whose master and slave images are recorded shortly before and after the event date.

Figure 10 shows the mean amplitude, with wrapped and unwrapped differential interferograms of the area affected by this tremor. The presence of fringes in the wrapped interferogram indicates the occurrence of a significant deformation. However, as PCRs were located at the edges of such fringe, no PS points were detected at the center of the fringe (see Figure 10c). The estimated unwrapped phase deviation is about 5.4 rad, which corresponds to a displacement of about 24 mm (obtained by multiplying the phase deviation times $\lambda/4\pi$, where λ is the radar wavelength of approximately 55.5 mm). This result agrees with that found in the displacement time series analysis. The co-seismic interferogram of the seismic event recorded in Pieszkowice on 30 July 2020 is shown in Figure 11. This event presents a higher intensity scale (equal to 3), a longer duration, but a reduced maximum ground acceleration regarding the previously analyzed event. A comparison between the two wrapped interferograms in Figures 10b and 11b reveals a higher number of fringes in the Pieszkowice interferogram, which also results in a larger estimated co-seismic phase deviation of about 12 rad, yielding a displacement of about 53 mm. The displacement time series in Figure 8d shows a phase-unwrapping error (positive jump) occurring during the July period. This error is probably related to a loss of coherence in the MTInSAR data (due to the seismic event itself) and causes a deviation from the GNSS LOS-projected time series. Phase unwrapping errors occur in InSAR data for a multitude of reasons and are associated with jumps in the accumulated phase time series of multiples of 2π (i.e., $\lambda/2$). In post-processing, an error correction was performed by subtracting 2π to the samples affected by the phase unwrapping error, yielding a corrected time series (Figure 12) that fits with the GNSS LOS-projected time series. The error correction was implemented by a trial-error procedure that first detects deviations that are close to a multiple of $\lambda/2$, then subtracts the correct multiple of $\lambda/2$ to the InSAR time series. The discontinuity of the corrected D_D time series is close to the one detected by the co-seismic analysis (about 53 mm). We also observe that, in this case, few PS points are detected close to the center of the fringe pattern in the differential interferogram, corresponding to strong scatterers, i.e., PCRs and buildings.

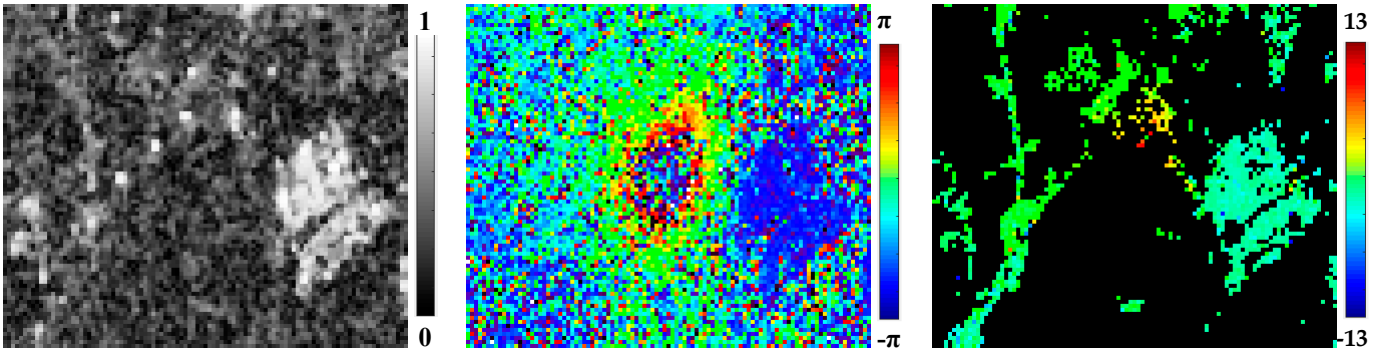

Figure 10. Mean amplitude (**a**), co-seismic wrapped (**b**) and unwrapped (**c**) interferograms of the Rudna mine area, in the vicinity of the WYZY GNSS station and seismometer. Master image: 19 July 2020. Slave image: 25 July 2020. Descending trajectory. Vertices of the area: [51°28.8′ N, 16°6′ E–51°29.4′ N, 16°3.6′ E]. Color scales: [0–1] (**a**), [$-\pi$, π] (**b**), [−13, 13] rad (**c**).

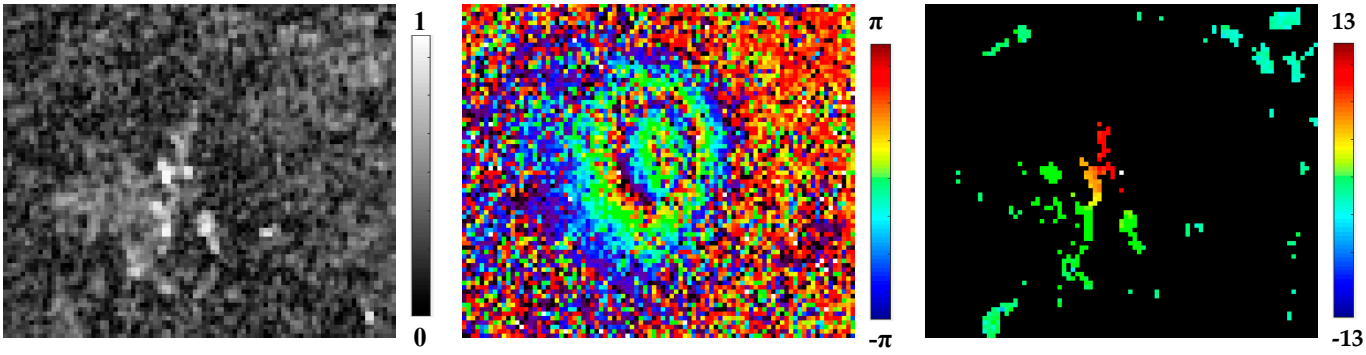

Figure 11. Mean amplitude (**a**), co-seismic wrapped (**b**), and unwrapped (**c**) interferograms of the Pieszkowice area in the vicinity of the PIES GNSS station and seismometer. Master image: 25 July 2020. Slave image: 31 July 2020. Descending trajectory. Vertices of the area: [51°28′ N, 16°9′ E–51°29.4′ N, 16°7.2′ E]. Color scales: [0–1] (**a**), [−π, π] (**b**), [−13, 13] rad (**c**).

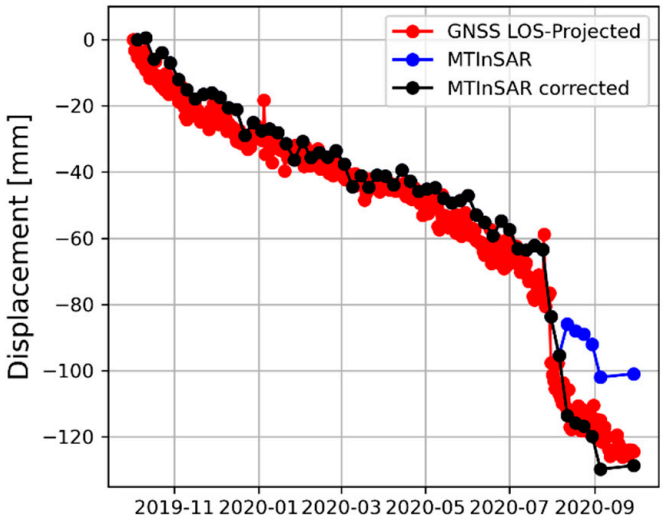

Figure 12. GNSS LOS-projected (red) and MTInSAR displacement time series for the PIES descending data. The phase unwrapping error in the original MTInSAR time series (blue) is corrected, yielding an error-free time series (black).

4.5. Vertical and Horizontal Deformation Components

The UD and EW deformation components extracted from the D_A and D_D LOS displacement datasets, using the method described in Section 3.2, are shown in Figure 13, displaying strong deformation rates. The UD component reaches maximum deformation values of about 30 mm in the Rudna mine (Polkowice south, marked with 1). Regarding the EW component, it is characterized by an area with positive values moving eastward (maximum deformation around 60 mm) which is close to an area displaying negative values moving westward (maximum deformation about 40 mm). A similar behavior, with significantly stronger deformation values, is observed in the area delimited by the towns of Przesieczna and Borów (about 7–8 km northwest of Polkowice, the area marked with indexes 3 and 4 and a black-dashed rectangle), as shown in Figure 14.

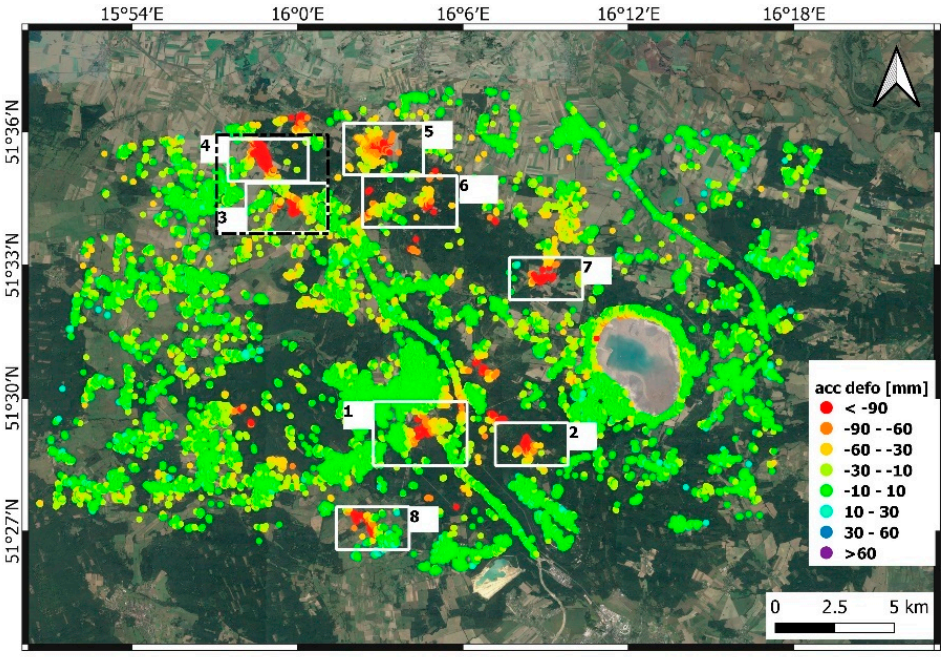

(**a**)

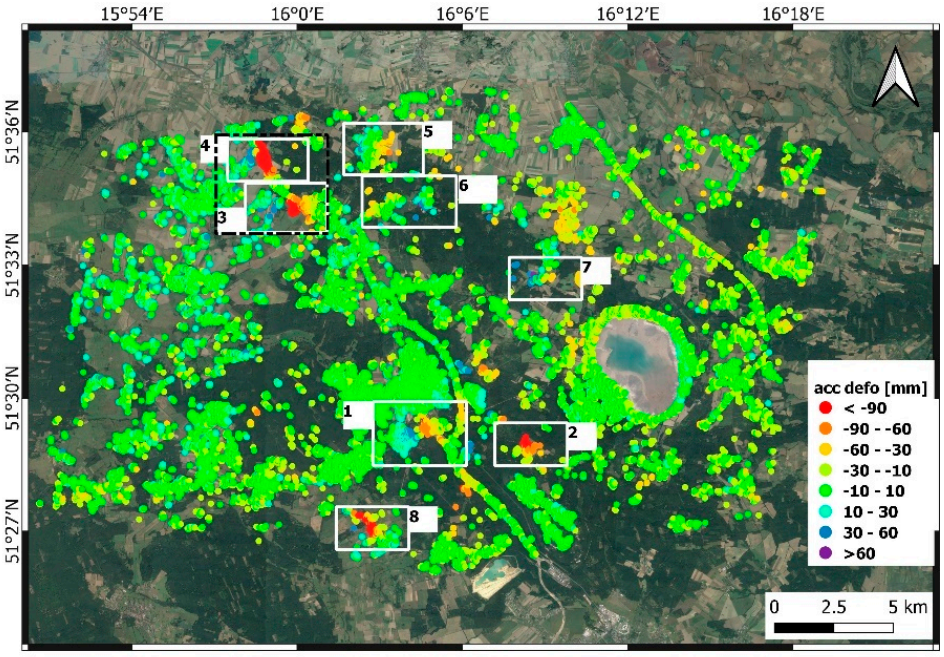

(**b**)

Figure 13. Up-down (**a**) and east-west (**b**) accumulated deformation maps of the area of interest.

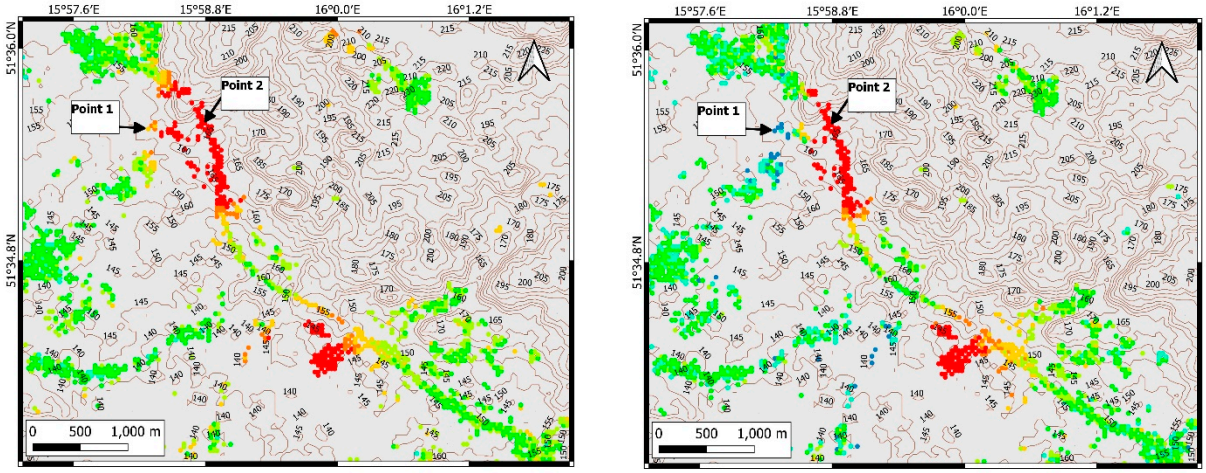

Figure 14. Up-down (**a**) and east-west (**b**) displacement maps of the area surrounding Przesieczna (area 3) and Borow (area 4), overlaid with the topographic contour lines of the selected area.

We observe two deformation spots moving in opposite directions on the EW deformation map. Two informative points were selected, belonging to each of these two patches, and their UD and EW deformation time series are shown in Figure 15. The UD component reaches a maximum of about −300 mm for point 2 and −80 mm for point 1, whereas the EW component has a maximum of about 250 mm eastward for point 2 and 60 mm westward for point 1. The deformation rates are approximately linear for both points. This behavior is probably related to the topography of the area. In order to provide more insight into this interpretation, the deformation maps in Figure 14 are overlaid with the topographic contour lines of the selected area. The contour map was computed from the digital elevation model provided by the Shuttle Radar Topography Mission (SRTM), with a resolution of 30 m. The slope of the area surrounding point 2 is not negligible: its estimated value is about 7° along the southwest direction, whereas point 1 is within an area with a smaller and opposite slope with respect to point 2. This topographic characteristic may well cause a horizontal deformation, as shown in Figures 14 and 15.

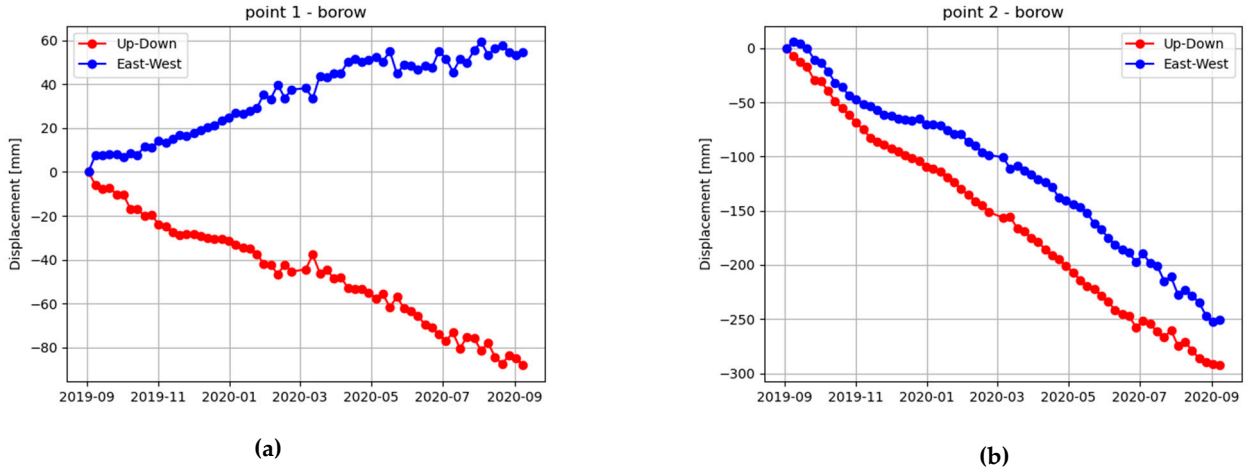

Figure 15. Time series of the extracted Up-Down (red) and East-West (blue) components associated with point 1 (**a**) and point 2 (**b**) in the deformation area surrounding Borow, as shown in Figure 12.

5. Discussion

The deformation maps depicted in Figure 6, for the LOS displacement data, and Figure 11, for the UD and EW deformation components, reveal that the point density is quite

high in urban and rural areas, whereas there is a lack of PSs in vegetated areas. Nevertheless, PS points are detected in most deformation areas, showing relevant displacements in many locations within the monitored surface. There is a limited number of points affected by phase unwrapping errors, as there are no wide areas affected by aliasing in the pre-APS filter maps. Noisy points seem to be isolated and do not affect the overall performance of the proposed procedure, which can be considered as an effect of the interferogram and point selection methods implemented. The employed technique shows good performance in detecting both slow linear deformation trends, as well as fast nonlinear ground motion phenomena (revealed also by in-situ seismometers and co-seismic interferogram analysis), which could be considered to be a relevant result for a model-free approach, such as the implemented one.

The LOS displacement time series are compared with the GNSS LOS-projected ones in Figure 8, showing an overall agreement, with significant deviations in a few cases. One of the causes of such deviations may be the misalignment between the detected points and the location of the GNSS station, in particular, in low-coherence areas. However, a relevant case is represented by the fast ground motion detected through the MTInSAR procedure in the Pieszkowice case (Figure 8d), confirmed by the seismometer data and the coseismic interferogram (Figure 11). A possible phase unwrapping error affects the MTInSAR D_D time series (shown in Figure 12), which is caused by a loss of coherence probably due to a strong seismic event (analyzed in Section 4.3). On the other hand, the discontinuities in the LOS displacement time series due to seismic events seem to be slightly lower than the displacements measured using the co-seismic differential interferograms and—if available-GNSS data. The smoothing functionality of the APS filter can be one of the causes of this performance loss. The APS temporal averaging functionality was tuned specifically to smooth abrupt changes due to atmospheric disturbances, which indeed may attenuate the effect of pulsed deformations. A fine-tuned pointwise APS temporal filter should be implemented to avoid this unwanted attenuation effect.

The UD and EW deformation maps highlighted the presence of two areas (south-Polkowice and Borów) divided into two sub-areas, one with an eastward and one with a westward horizontal component. The main factor causing the opposite behavior of the horizontal components is the topography and the difference in the slopes between two nearby spots. However, the presence of strong horizontal components in mining-induced deformations was studied in [6,26] and may be due to a rotational ground motion component, triggered by underground excavation and also related to the geological properties of the areas.

6. Conclusions

This work has investigated a study on both slow and fast ground motion phenomena induced by underground mining activity using a MTInSAR method that implements a fast interferogram and the point selection technique, followed by a spatio-temporal filtering stage to mitigate the effect of the atmospheric disturbances. The interferogram selection method applies a dual condition to the minimum average coherence of each interferogram forming the network, and the minimum redundancy of each image in the analyzed stack. The APS filter is based on an NFFT that processes the non-uniform grid of points in order to perform the spatial filtering in the frequency domain, which is followed by a temporal filter to eliminate abrupt changes due to the atmospheric disturbance. The proposed method was applied to two stacks of Sentinel-1 SAR SLC images in descending and ascending orbits, aiming at monitoring the deformations caused by underground mining activity in the Legnica-Glogow copper district, Lower Silesian region, Poland.

The adopted method has shown good performance in detecting slow linear deformation as well as pulse events due to tremors triggered by underground mining activity. Validation was performed by comparing the results obtained from the Sentinel-1 data with in-situ measurements performed with GNSS and seismometers devices.

However, the presence of noisy PS points was noticed in the ascending/descending LOS displacement maps, as well as in the vertical/horizontal deformation maps. In the adopted method, the filtering of the noise component in the wrapped interferogram was performed using a multilook window, which intrinsically decreases the spatial resolution of the data. With the aim of improving the noise mitigation capabilities of this method, an interferogram filtering stage will be added in future works, based either on traditional approaches, e.g., the Goldstein filter [14], or more complex ones, such as the one proposed in [17]. It should be noted that some design choices made to develop the MTInSAR technique are linked to the characteristics of the AOI. The studied area presents a quasi-flat topography—apart from a few spots—which renders negligible two otherwise significant sources of error in InSAR data, i.e., the residual topographic error and the stratified delay component of the APS. On the other hand, significant decorrelation phenomena due to the environmental characteristics of the AOI, i.e., snow (January–February) and vegetation growth (June–July) were noticed. We adopted a simple interferogram elimination criterion to tackle the temporal decorrelation issues of the AOI.

Future developments of this work will aim at assessing the performance of the adopted method in terms of the existing ones [17,19]. Quality indicators for the obtained products, e.g., [44], can be employed to provide further validation and to optimally tune the main algorithm parameters, i.e., minimum average coherence, minimum image redundancy, and the threshold for the equivalent spatial coherence used for the point selection. The study of the displacement time series has revealed the presence of abrupt changes due to the seismic activity that are extremely dangerous for the built environment and infrastructures. Thorough, rapid monitoring of such issues is often necessary and can benefit from automated procedures to detect and classify deformation time series that exhibit discontinuities or trend changes [21,45,46], which can be successfully tackled using machine learning tools [47].

Author Contributions: Conceptualization: R.P. and M.C.; methodology, R.P., M.C., A.B. and O.M.; software, R.P., O.M. and B.C.; validation, R.P., J.R., M.M. (Marek Mróz), N.K. and M.M. (Magdalena Mleczko); writing—original draft preparation, R.P.; writing—review and editing, M.C., J.R., A.B. and M.C.-G.; visualization, R.P., A.B. and M.C.-G.; supervision, M.C. All authors have read and agreed to the published version of the manuscript.

Funding: This work is part of the Spanish Grant SARAI, PID2020-116540RB-C21, funded by MCIN/AEI/10.13039/501100011033. This research was partially conducted under the project titled Automatic System for Monitoring the Influence of High-Energy Paraseismic Tremors on the Surface Using GNSS/PSInSAR Satellite Observations and Seismic Measurements (Project No. POIR.04.01.04-00-0056/17), co-financed from the European Regional Development Fund within the Smart Growth Operational Program 2014–2020.

Data Availability Statement: Datasets are available at the Geomatics Research Unit of the Centre Tecnològic de Telecomunicacions de Catalunya, CTTC.

Acknowledgments: The authors of the study would like to thank the European Space Agency (ESA) for providing Sentinel-I SAR data free of charge. The authors are also grateful to the QGIS team for the free and open-source software used to create some of the maps of this study.

Conflicts of Interest: The authors declare no conflict of interest.

References

1. Owczarz, K.; Blachowski, J. Application of DInSAR and spatial statistics methods in analysis of surface dis-placements caused by induced tremors. *Appl. Sci.* **2020**, *10*, 7660. [CrossRef]
2. Sopata, P.; Stoch, T.; Wójcik, A.; Mrocheń, D. Land Surface Subsidence Due to Mining-Induced Tremors in the Upper Silesian Coal Basin (Poland)—Case Study. *Remote Sens.* **2020**, *12*, 3923. [CrossRef]
3. Malinowska, A.A.; Witkowski, W.T.; Guzy, A.; Hejmanowski, R. Mapping ground movements caused by min-ing-induced earthquakes applying satellite radar interferometry. *Eng. Geol.* **2018**, *246*, 402–411. [CrossRef]
4. Witkowski, W.T.; Łukosz, M.; Guzy, A.; Hejmanowski, R. Estimation of Mining-Induced Horizontal Strain Tensor of Land Surface Applying InSAR. *Minerals* **2021**, *11*, 788. [CrossRef]

5. Hejmanowski, R.; Witkowski, W.T.; Guzy, A.; Malinowska, A. Identification of the ground movements caused by mining-induced seismicity with the satellite interferometry. *Proc. Int. Assoc. Hydrol. Sci.* **2020**, *382*, 297–301. [CrossRef]
6. Antonielli, B.; Sciortino, A.; Scancella, S.; Bozzano, F.; Mazzanti, P. Tracking Deformation Processes at the Legnica Glogow Copper District (Poland) by Satellite InSAR—I: Room and Pillar Mine District. *Land* **2021**, *10*, 653. [CrossRef]
7. Mazzanti, P.; Antonielli, B.; Sciortino, A.; Scancella, S.; Bozzano, F. Tracking Deformation Processes at the Legnica Glogow Copper District (Poland) by Satellite InSAR—II: Żelazny Most Tailings Dam. *Land* **2021**, *10*, 654. [CrossRef]
8. Jing-Xiang, G.; Hong, H. Advanced GNSS technology of mining deformation monitoring. *Procedia Earth Planet. Sci.* **2009**, *1*, 1081–1088. [CrossRef]
9. Zhou, D.; Wu, K.; Chen, R.; Li, L. GPS/terrestrial 3D laser scanner combined monitoring technology for coal mining subsidence: A case study of a coal mining area in Hebei, China. *Nat. Hazards* **2013**, *70*, 1197–1208. [CrossRef]
10. Massonnet, D.; Feigl, K.L. Radar interferometry and its application to changes in the Earth's surface. *Rev. Geophys.* **1998**, *36*, 441–500. [CrossRef]
11. Moreira, A.; Prats-Iraola, P.; Younis, M.; Krieger, G.; Hajnsek, I.; Papathanassiou, K.P. A tutorial on synthetic ap-erture radar. *IEEE Geosci. Remote Sens. Mag.* **2013**, *1*, 6–43. [CrossRef]
12. Ferretti, A.; Prati, C.; Rocca, F. Permanent scatterers in SAR interferometry. *IEEE Trans. Geosci. Remote Sens.* **2001**, *39*, 8–20. [CrossRef]
13. Crosetto, M.; Monserrat, O.; Cuevas-González, M.; Devanthéry, N.; Crippa, B. Persistent Scatterer Interferometry: A Review. *ISPRS J. Photogramm. Remote Sens.* **2016**, *115*, 78–89. [CrossRef]
14. Goldstein, R.M.; Werner, C.L. Radar interferogram filtering for geophysical applications. *Geophys. Res. Lett.* **1998**, *25*, 4035–4038. [CrossRef]
15. Hooper, A.; Bekaert, D.; Spaans, K.; Arıkan, M. Recent advances in SAR interferometry time series analysis for measuring crustal deformation. *Tectonophysics* **2012**, *514–517*, 1–13. [CrossRef]
16. Ferretti, A.; Fumagalli, A.; Novali, F.; Prati, C.; Rocca, F.; Rucci, A. A New Algorithm for Processing Interferometric Data-Stacks: SqueeSAR. *IEEE Trans. Geosci. Remote Sens.* **2011**, *49*, 3460–3470. [CrossRef]
17. Pepe, A.; Yang, Y.; Manzo, M.; Lanari, R. Improved EMCF-SBAS Processing Chain Based on Advanced Techniques for the Noise-Filtering and Selection of Small Baseline Multi-Look DInSAR Interferograms. *IEEE Trans. Geosci. Remote Sens.* **2015**, *53*, 4394–4417. [CrossRef]
18. Refice, A.; Bovenga, F.; Nutricato, R. MST-based stepwise connection strategies for multipass radar data, with application to coregistration and equalization. IEEE Trans. *Geosci. Remote Sens.* **2006**, *44*, 2029–2040. [CrossRef]
19. Perissin, D.; Wang, T. Repeat-Pass SAR Interferometry with Partially Coherent Targets. *IEEE Trans. Geosci. Remote. Sens.* **2011**, *50*, 271–280. [CrossRef]
20. Crippa, C.; Valbuzzi, E.; Frattini, P.; Crosta, G.B.; Spreafico, M.C.; Agliardi, F. Semi-automated regional classifica-tion of the style of activity of slow rock-slope deformations using PS InSAR and SqueeSAR velocity data. *Landslides* **2021**, *18*, 2445–2463. [CrossRef]
21. Raspini, F.; Bianchini, S.; Ciampalini, A.; Del Soldato, M.; Solari, L.; Novali, F.; Del Conte, S.; Rucci, A.; Ferretti, A.; Casagli, N. Continuous, semi-automatic monitoring of ground deformation using Sentinel-1 satellites. *Sci. Rep.* **2018**, *8*, 7253. [CrossRef] [PubMed]
22. Crosetto, M.; Solari, L.; Mróz, M.; Balasis-Levinsen, J.; Casagli, N.; Frei, M.; Oyen, A.; Moldestad, D.; Bateson, L.; Guerrieri, L.; et al. The Evolution of Wide-Area DInSAR: From Regional and National Services to the European Ground Motion Service. *Remote Sens.* **2020**, *12*, 2043. [CrossRef]
23. Manunta, M.; De Luca, C.; Zinno, I.; Casu, F.; Manzo, M.; Bonano, M.; Fusco, A.; Pepe, A.; Onorato, G.; Berardino, P.; et al. The Parallel SBAS Approach for Sentinel-1 Interferometric Wide Swath Deformation Time-Series Generation: Algorithm Description and Products Quality Assessment. *IEEE Trans. Geosci. Remote Sens.* **2019**, *57*, 6259–6281. [CrossRef]
24. Cigna, F.; Tapete, D. Sentinel-1 Big Data Processing with P-SBAS InSAR in the Geohazards Exploitation Platform: An Experiment on Coastal Land Subsidence and Landslides in Italy. *Remote Sens.* **2021**, *13*, 885. [CrossRef]
25. Solari, L.; Montalti, R.; Barra, A.; Monserrat, O.; Bianchini, S.; Crosetto, M. Multi-Temporal Satellite Interferometry for Fast-Motion Detection: An Application to Salt Solution Mining. *Remote Sens.* **2020**, *12*, 3919. [CrossRef]
26. Pawluszek-Filipiak, K.; Borkowski, A. Integration of DInSAR and SBAS techniques to determine mining-related deformations using Sentinel-1 data: The case study of rydultowy mine in Poland. *Remote Sens.* **2020**, *12*, 242. [CrossRef]
27. Przylucka, M.; Herrera, G.; Graniczny, M.; Colombo, D.; Béjar-Pizarro, M. Combination of conventional and ad-vanced DInSAR to monitor very fast mining subsidence with TerraSAR-X data: Bytom City (Poland). *Remote Sens.* **2015**, *7*, 5300–5328. [CrossRef]
28. Devanthéry, N.; Crosetto, M.; Monserrat, O.; Cuevas-González, M.; Crippa, B. The PSIG chain: An approach to Persistent Scatterer Interferometry. *SAR Image Anal. Model. Tech. XIV* **2014**, *9243*, 92430K.
29. Devanthéry, N.; Crosetto, M.; Monserrat, O.; Cuevas-González, M.; Crippa, B. An Approach to Persistent Scatterer Interferometry. *Remote Sens.* **2014**, *6*, 6662–6679. [CrossRef]
30. Hanssen, R.F. *Radar Interferometry: Data Interpretation and Error Analysis*; Kluwer Academic Publishers: Dordrecht, The Netherlands, 2001.
31. Van Leijen, F. Persistent Scatterer Interferometry Based on Geodetic Estimation Theory. Ph.D. Thesis, Delft University of Technology, Delft, The Netherlands, 2014. [CrossRef]

32. Ferretti, A.; Prati, C.; Rocca, F. Nonlinear Subsidence Rate Estimation Using permanent scatterers in differential SAR interferometry. *IEEE Trans. Geosci. Remote Sens.* **2000**, *38*, 2202–2212. [CrossRef]
33. Kunis, S. Nonequispaced FFT, Generalisation and Inversion. Ph.D. Thesis, University of Lubeck, Lubeck, Germany, 2006.
34. Fuhrmann, T.; Garthwaite, M.C. Resolving Three-Dimensional Surface Motion with InSAR: Constraints from Multi-Geometry Data Fusion. *Remote Sens.* **2019**, *11*, 241. [CrossRef]
35. Ulaby, F.T.; Long, D.G. *Microwave Radar and Radiometric Remote Sensing*; The University of Michigan Press: Ann Arbor, MI, USA, 2014.
36. Zebker, H.; Villasenor, J. Decorrelation in interferometric radar echoes. *IEEE Trans. Geosci. Remote Sens.* **1992**, *30*, 950–959. [CrossRef]
37. Yu, H.; Lan, Y.; Yuan, Z.; Xu, J.; Lee, H. Phase Unwrapping in InSAR: A Review. *IEEE Geosci. Remote Sens. Mag.* **2019**, *7*, 40–58. [CrossRef]
38. Costantini, M. A novel phase unwrapping method based on network programming. *IEEE Trans. Geosci. Remote Sens.* **1998**, *36*, 813–821. [CrossRef]
39. Keiner, J.; Kunis, S.; Potts, D. Using NFFT 3—A software library for various nonequispaced fast fourier trans-forms. *ACM Trans. Math. Softw.* **2009**, *36*, 1–23. [CrossRef]
40. Palama, R.; Crosetto, M.; Monserrat, O.; Barra, A.; Cuevas, M.; Crippa, B.; Rapinski, J.; Mroz, M. Filtering of the atmospheric phase screen in InSAR data using the Nonequispaced Fast Fourier Transform. In Proceedings of the 2021 IEEE International Geoscience and Remote Sensing Symposium IGARSS, Brussels, Belgium, 11–16 July 2021; pp. 3979–3982. [CrossRef]
41. Navarro, J.A.; Tomas, R.; Barra, A.; Pagán, J.I.; Reyes-Carmona, C.; Solari, R.; Vinielles, J.L.; Falco, S.; Crosetto, M. ADAtools: Automatic detection and classification of active deformation areas from PSI dis-placement maps. *ISPRS Int. J. Geo-Inf.* **2020**, *9*, 584. [CrossRef]
42. Stepniak, K.; Baryła, R.; Wielgosz, P.; Kurpinski, G. Optimal data processing strategy in precise GPS leveling net-works. *Acta Geodyn. Geromater.* **2013**, *10*, 443–452. [CrossRef]
43. Wodynski, A.; Lasocki, S. Assessment of mining tremor influence on the technical wear of building. *Acta Geodyn. Geomater.* **2004**, *1*, 187–194.
44. Wassie, Y.; Mirmazloumi, S.M.; Crosetto, M.; Palamà, R.; Monserrat, O.; Crippa, B. Spatio-Temporal Quality Indi-cators for Differential Interferometric Synthetic Aperture Radar Data. *Remote Sens.* **2022**, *14*, 798. [CrossRef]
45. Berti, M.; Corsini, A.; Franceschini, S.; Iannacone, J.P. Automated classification of Persistent Scatterers Interfer-ometry time series. *Nat. Hazards Earth Syst. Sci.* **2013**, *13*, 1945–1958. [CrossRef]
46. Mirmazloumi, S.M.; Wassie, Y.; Navarro, J.A.; Palamà, R.; Krishnakumar, V.; Barra, A.; Cuevas-González, M.; Crosetto, M.; Monserrat, O. Classification of ground deformation using sentinel-1 persistent scatterer interferometry time series. *GISci. Remote Sens.* **2022**, *59*, 374–392. [CrossRef]
47. Ansari, H.; Rubwurm, M.; Ali, M.; Montazeri, S.; Parizzi, A.; Zhu, X.X. InSAR Displacement Time Series Mining: A Machine Learning Approach. In Proceedings of the International Geoscience and Remote Sensing Symposium (IGARSS 2021), Brussels, Belgium, 11–16 July 2021; Volume 4, pp. 3301–3304.